Research Article | Vol. 30, No. 18 / 29 Aug 2022 / Optics Express 33035
Optics EXPRESS

Interfacial topological photonics: broadband silicon waveguides for THz 6G communication and beyond

YI JI TAN,[1,2,3] WENHAO WANG,[1,2,4] ABHISHEK KUMAR,[1,2] AND RANJAN SINGH[1,2,*]

[1]*Division of Physics and Applied Physics, School of Physical and Mathematical Sciences, Nanyang Technological University, 21 Nanyang Link, Singapore 637371, Singapore*
[2]*Centre for Disruptive Photonic Technologies, School of Physical and Mathematical Sciences, Nanyang Technological University, 21 Nanyang Link, Singapore 637371, Singapore*
[3]*Agency for Science, Technology and Research, 1 Fusionopolis Way, Connexis North Tower, Singapore 138632, Singapore*
[4]*Institute of Fundamental and Frontier Sciences, University of Electronic Science and Technology of China, Chengdu 610054, China*
[*]*ranjans@ntu.edu.sg*

Abstract: Topological photonics has expanded our understanding of electromagnetic wave propagation and unraveled new methods of electromagnetic wave shaping. Among the various topological photonic systems, valley photonic crystal (VPC) is a highly versatile platform for constructing interfaces that supports unidirectional edge state to enable the robust topological transport of light. Although silicon VPC waveguides has demonstrated the lossless propagation of terahertz (THz) waves through multiple sharp bends, existing designs are mostly based on the standard zigzag-interface. Here, we explore interfacial topological photonics by designing a composite interface junction for an air-slot-like VPC waveguide with a 60° bend and an unchanging bearded-interface to allow the topologically protected propagation of THz waves over a 20% relative bandwidth. We employ particle swarm optimization to design the geometry of a bearded-interface silicon VPC waveguide to achieve a 42% relative bandgap and a topological edge state spanning a usable 25% relative bandwidth. Our work illustrates the prospects and challenges of interfacial topological photonics in the design of broadband silicon topological waveguides for potential applications across the electromagnetic spectrum, including the on-chip THz sixth-generation (6G) communication.

1. Introduction

The emergence of data-hungry applications such as virtual reality, augmented reality, and holographic communications have fueled the demand for extremely high data rates [1–3]. Consequently, wireless communication standards are gradually moving towards the terahertz regime as predicted by Edholm's law [4]. The THz band (from 0.1 to 10 THz) is thus envisioned as the key enabler for 6G wireless communication [5,6], where its wide bandwidth availability has the potential to realize wireless communication with terabits-per-second data rates. However, the realization of THz wireless communication is limited by the lack of high-power THz sources, mainly due to the low conversion efficiency of antenna at THz frequencies [7]. In addition, conventional metallic THz interconnects are lossy and can only support relatively low bandwidth [8]. Therefore, the development of low-loss and broadband THz integrated circuits is needed to counteract the limited available power of existing THz sources and to efficiently integrate the emerging THz communication devices [9].

To enable on-chip THz communications, it is necessary to develop efficient THz integrated circuits, which requires robust and lossless THz photonic waveguides. Metallic waveguides

#468010 https://doi.org/10.1364/OE.468010
Journal © 2022 Received 15 Jun 2022; revised 25 Jul 2022; accepted 29 Jul 2022; published 25 Aug 2022

Optics EXPRESS

suffer from ohmic losses at high frequencies and are not suitable for THz integrated circuits. Silicon photonics on the other hand has gained popularity due to its low loss properties, where high-resistivity silicon has been used to design photonic crystal waveguides with negligible propagation losses at THz frequencies [10–13]. Furthermore, silicon THz integrated circuits can be fabricated in a large-scale single etching process that is cost-effective and compatible with the existing complementary metal-oxide semiconductor (CMOS) fabrication technology. The waveguiding property in photonic crystals is achieved by utilizing the photonic bandgap, which forbids the propagation of electromagnetic waves in the photonic crystal. However, it remains a challenge to simultaneously achieve low loss and broadband dispersion control at THz frequencies for typical photonic crystal waveguides [14].

The recent introduction of topological photonics revealed additional degrees of freedom in light propagation and offers an alternative approach of manipulating electromagnetic waves [15]. For instance, the interface between two distinct photonic topological insulators (PTIs) can support unidirectional edge state that allow robust and reflectionless wave propagation [16,17]. Topological photonics has been explored in other platforms such as topological polaritonics which offers additional degrees of freedom for exotic light matter interactions, such as the observation of topological exciton polaritons and phonon-polariton in two-dimensional (2D) metasurfaces [18,19]. In addition, the discovery of valley edge states in 2D photonic crystal has enabled the construction of robust and lossless silicon waveguide [20,21]. Silicon VPC waveguide has also demonstrated the near-unity transmission of THz waves above the 300 GHz band along multiple sharp bends [22]. Unlike the photonic crystal bandgap which arises due to Bragg reflections, the photonic bandgap in VPCs results from the breaking of inversion symmetry via the introduction of asymmetrical air holes in the VPC unit cell. The negligible propagation and bending loss in VPC waveguides are attributed to the topologically protected edge states provided by the bulk VPC on either side of the interface. In addition, the linear dispersion of topological edge states in VPC waveguides allow the entire bandwidth to be used for on-chip communication with minimal signal delay across different frequencies [22,23]. While there have been some studies on the geometrical optimization of air holes in VPCs [24,25], existing designs of VPC waveguides still show a limited 8% relative bandwidth utilization [26]. Further optimization and interfacial engineering of the VPC waveguides would allow the linear dispersion of topological edge states to be exploited over a larger relative bandwidth to realize broadband THz on-chip communications.

Here, we employ interfacial topological photonics to design a composite interface junction to allow the robust topological transport of broadband THz waves along a 60° bend with an unchanging bearded-interface in an air-slot VPC waveguide, showing high transmittance over a 20% relative bandwidth. The silicon VPC waveguide is optimized via the particle swarm algorithm by varying the shape and size (number of vertices and radii) of equilateral polygon air holes in rhombus unit cells arranged to form a bearded-interface. Our optimized VPC structure comprises of two dodecagon (12-sided polygon) air holes with extreme asymmetrical sizes in a rhombus unit cell, which achieved more than 42% relative bandgap. The optimized silicon VPC waveguide also supports a broadband topological edge state which spans a usable 25% relative bandwidth below the light line outside the leaky region. Our design method is scalable across the electromagnetic spectrum, ranging from microwave to optical regimes, limited mainly by the availability of low-loss high-refractive index materials and the associated fabrication constrains. In addition, we provide a comprehensive study to illustrate the effect of air hole geometry on the relative bandgap and the relative bandwidth spanned by the topological edge states of silicon VPC waveguides with bearded-interface. Using VPCs as a platform, we have uncovered interfacial topological photonics as a new approach to design broadband silicon waveguides for realizing THz topological integrated devices in 6G communications, as well as topological waveguide cavities for THz sensing applications.

Optics EXPRESS

2. Results

2.1. Broadband THz topological silicon waveguide based on VPCs

In this section, we present a broadband THz topological planar waveguide based on 2D VPCs constructed using silicon slab of 200 μm thickness. To reduce computation requirements for bandwidth optimization, the electromagnetic simulation in this work is performed in 2D by employing a variational method that approximates the 2D effective refractive index of photonic crystal slabs [27]. This approximation assumes negligible coupling between the vertical slab modes supported by the refractive index profile of the three-dimensional (3D) slab waveguide, which is satisfied for in-plane waveguide modes with subluminal phase velocity. For a 200 μm thick silicon slab in free space, the 2D effective refractive index is approximated as $n_{\text{eff}} = 3.0$ across the THz frequencies.

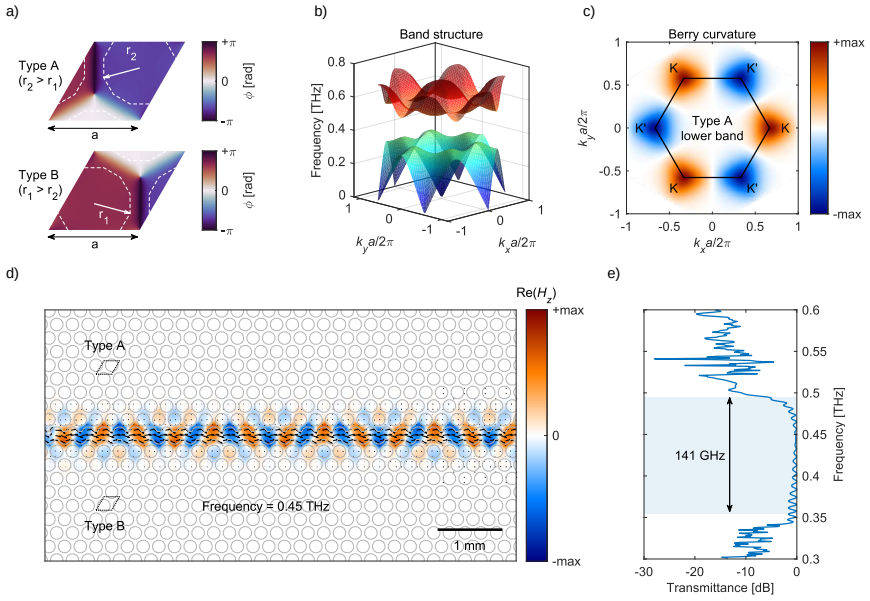

Fig. 1. Broadband THz topological silicon waveguide based on VPCs. (a) Rhombus unit cells of VPC with lattice constant $a = 242.5$ μm and dodecagon (12-sided polygon) air holes of radius $r_1 = 0$ and $r_2 = 0.408a$. The colormap represents the phase distribution of the magnetic field (H_z) at the K' valleys of the lower band frequency for Type A ($r_2 > r_1$) and Type B ($r_1 > r_2$) unit cell, showing opposing magnetic phase vortices. (b) Band structure of the VPC, showing a 193 GHz photonic bandgap centered at 451 GHz. (c) Berry curvature of the lower band for Type A unit cell. (d) Magnetic field profile (H_z) of a topological waveguide constructed using the VPC in (a) with a bearded-interface. The quiver plot represents the time-averaged power flow of the electromagnetic fields. (e) Simulated transmission spectrum of the optimized VPC waveguide, showing a high transmittance across the topological edge state bandwidth.

Figure 1 shows the magnetic field profile (H_z) of a broadband THz topological VPC waveguide as well as the magnetic phase vortex, band structure and Berry curvature of the VPC unit cell for the transverse electric (TE) mode. The unit cell has a lattice constant of $a = 242.5$ μm with just a single dodecagon air hole ($r_1 = 0$, $r_2 = 0.408a$) as shown in Fig. 1(a). The magnetic field phase vortex calculated at the K' valley for the lower frequency band is also shown in Fig. 1(a). The magnetic phase vortex shows a full 2π clockwise rotation of increasing phase about the air hole with radius r_1 for Type A unit cell and an anti-clockwise phase rotation at the air hole of

Optics EXPRESS

radius r_2 for Type B unit cell. The asymmetrically-sized air holes, where in this case one is completely removed, results in the inversion symmetry breaking of the photonic crystal structure which opens an indirect bandgap as shown in Fig. 1(b) (also in Fig. 2(b)). To ensure that the VPC unit cell can offer topological protection of the edge states, we numerically calculate the Berry curvature [28] at the lower band (Fig. 1(c)), showing the localization of Berry curvature around the K and K' valleys with opposing signs. The time-reversal symmetry of the VPC is given by the symmetrical distribution of Berry curvature, resulting in a zero Chern number when integrated over the entire Brillouin zone. Meanwhile, the valley Chern numbers are non-zero and their sign depends on the choice of unit cell (Type A or Type B) and valleys (K or K'), which is dependent on the chirality of magnetic phase vortex.

While VPC waveguides are often designed using the standard zigzag-interface, we use the bearded-interface (as described in several studies [29–31]) to construct a broadband THz topological waveguide. Figure 1(d) illustrates the magnetic field profile of the VPC waveguide excited with a unidirectional TE dipole array source at 0.45 THz frequency, showing a highly confined magnetic field that propagates along the asymmetric air-slot waveguide resulting from the bearded-interface. The VPC waveguide shows high transmittance across a 141 GHz bandwidth of the topological edge state within the bandgap as depicted in Fig. 1(e), with a usable 114 GHz bandwidth below the light line with subluminal phase velocity.

2.2. Bandwidth optimization of topological edge state in VPC waveguide

The VPC waveguide structure in Fig. 1 is designed via the particle swarm optimization [32] to maximize the bandgap ratio (ratio of the bandgap Δf to the mid-gap frequency f_0) and relative bandwidth (ratio of the bandwidth Δf_1 to mid-gap frequency f_0) of the topological edge state by varying the shape and size of the air holes in a VPC rhombus unit cell. We consider air holes in the shape of equilateral polygons with number of vertices (v) given in the multiple of 3, and varying radii (r_1 and r_2) within the range $[0, a/\sqrt{3}]$. We only consider the bearded-interface since the VPC waveguide for a zigzag-interface has already been optimized to a considerable extent, where the intersection between the topological edge state and light line matches the valence frequency of the photonic bandgap to give an 8% relative bandwidth [22].

Figure 2 illustrates the bandwidth optimization of VPC waveguides with a bearded-interface. Both the hexagon lattice and rhombus unit cell of the optimized VPC is depicted in Fig. 2(a), where the bearded-interface is lined out in blue with Type A unit cells in the upper half and Type B unit cells in the lower half region. The optimized VPC unit cell has an indirect bandgap of 193 GHz centered at 451 GHz frequency as shown in the band structure calculated along the high symmetry lines (Fig. 2(b)), which corresponds to a 42.8% bandgap ratio. Figure 2(c) shows the projected band diagram of the VPC waveguide unit cell, where the colored filled region (orange and blue) consists of the bulk states, with topological edge states represented by the colored lines. The topological edge state (orange line) spans a bandwidth of 178 GHz extending beyond the bandgap (grey region) of which 114 GHz (25.3% relative bandwidth) are below the light line. In addition, the usable 114 GHz bandwidth exhibits an approximately linear dispersion of light which is highly desirable for on-chip THz data communications.

The band diagram in Figs. 2(b) and 2(c) are calculated using the plane wave expansion method (see Methods), where each eigenfrequency are indexed based on the number of plane waves used. The well-defined frequency band indices allow the systematic identification and calculation of the bandgap and bandwidth of topological edge states where the objective function can be implemented in a straightforward manner for particle swarm optimization. As a result, the bandwidth calculated from the indexed eigenfrequencies of a topological edge state can return a non-zero value even when there is no bandgap. We circumvent this limitation by defining the objective function as a product of bandgap ratio ($\Delta f/f_0$) and the topological edge state relative bandwidth ($\Delta f_1/f_0$), given by $\Delta f \Delta f_1/f_0^2$. The advantage of such figure of merit (FOM) is clear,

Optics EXPRESS

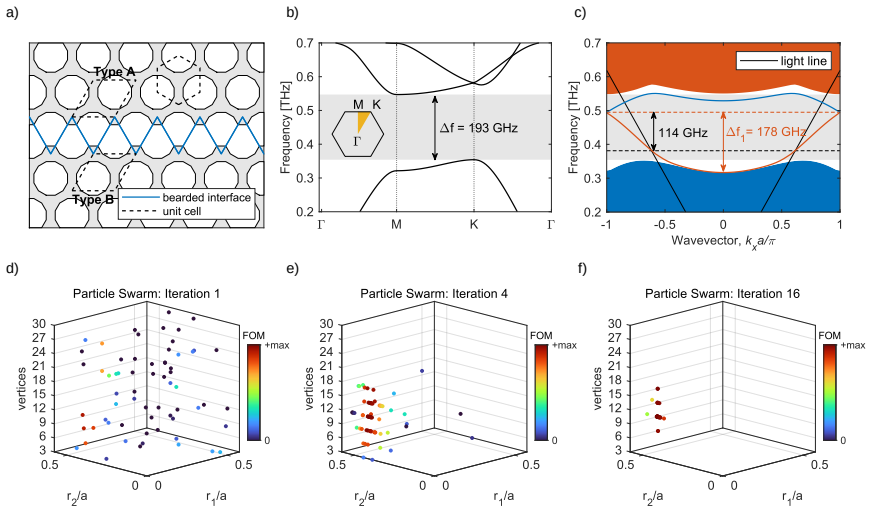

Fig. 2. Bandwidth optimization of topological edge state. (a) Optimized bearded-interface VPC waveguide with dodecagon air holes of radii $r_1 = 0$ and $r_2 = 0.408a$, showing region of silicon (grey) and air (white). (b) Band structure of the optimized VPC unit cell along the high symmetry lines, showing a photonic bandgap of $\Delta f = 193$ GHz centered at $f_0 = 451$ GHz. (c) Projected band diagram of the optimized VPC waveguide, with a topological edge state (orange line) spanning a bandwidth of $\Delta f_1 = 178$ GHz beyond the bandgap into the bulk states. The usable bandwidth of this topological edge state spans 114 GHz below the light line. (d)-(f) Evolution of the particle swarm in 3D parameter space (number of vertices and radii of equilateral polygon air holes), showing convergence towards an optimal solution using a figure of merit (FOM) defined as the product of bandgap ratio ($\Delta f / f_0$) and topological edge state relative bandwidth ($\Delta f_1 / f_0$).

since the objective function is maximum at $\Delta f = \Delta f_1$, where the bandgap is fully utilized by the topological edge state. In addition, maximizing Δf_1 increase the group velocity and the usable bandwidth of the topological edge state that falls below the light line.

Figures 2(d) to 2(f) shows the evolution of a swarm of 64 particles that are randomly initialized in the 3D parameter space, where the color of each particle represents the objective function value. Using an inertia coefficient of 0.5, cognitive coefficient of 1.5 and a social coefficient of 1.5, the particle swarm converged towards an optimal value after just 16 iterations (see Methods). In addition, the objective function of $\Delta f \Delta f_1 / f_0^2$ as a dimensionless quantity suggests that the optimized VPC structure is equally valid for unit cells of varying lattice constant with the condition that the 2D effective refractive index of the 200 μm thick silicon slab remains unchanged for the desired frequency bandwidth. The topological edge state can therefore be tuned to span the same relative bandwidth at other frequency bands simply by scaling the lattice constant and air hole sizes of the optimized VPC structure.

2.3. *Effects of air hole geometry on the bandgap and the topological edge state bandwidth of silicon VPC waveguides*

Figure 3 shows how the bandgap ratio ($\Delta f / f_0$) of VPCs vary with the air holes shape (equilateral polygons with v vertices) and radii (r_1 and r_2) in a rhombus unit cell of period $a = 242.5$ μm. The bandgap ratio is enhanced significantly when the air hole shape are equilateral polygons with 6 or more vertices, exhibiting up to 44% bandgap ratio for hexagonal air holes. In addition, the bandgap ratio is maximized when one air hole is completely removed ($r_1 = 0$ or $r_2 = 0$). Figure 3 also shows that the photonic bandgap arises due to the inversion symmetry breaking ($r_1 \neq r_2$).

Optics EXPRESS

Figures 3(d) to 3(f) show the photonic bandgap as a function of air hole asymmetry corresponding to the white dashed line in Figs. 3(a), 3(b), and 3(c), respectively.

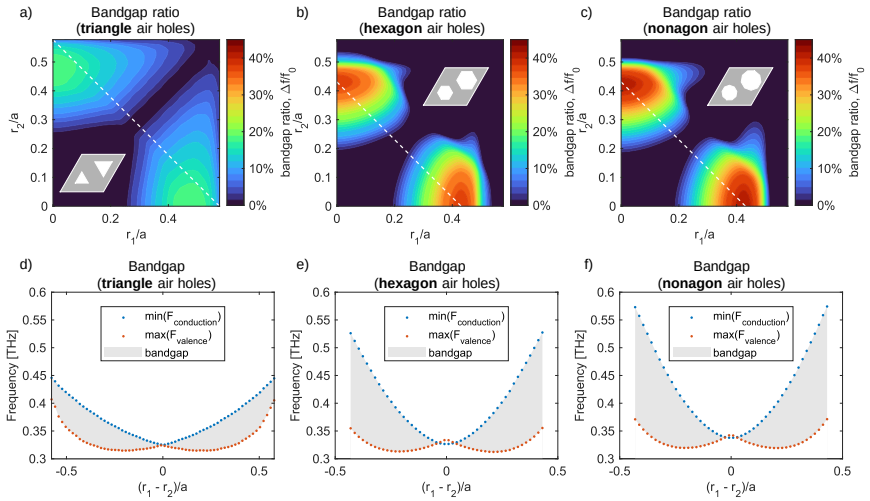

Fig. 3. Bandgap of VPCs as a function of air hole radii (r_1, r_2) for equilateral (a) triangular holes, (b) hexagonal holes, and (c) nonagonal holes. The bandgap is given by $\Delta f = f_c - f_v$ where $f_c = \min(F_{\text{conduction}})$ and $f_v = \max(F_{\text{valence}})$. (d)-(f) The conduction and valence band plotted as a function of air hole radius difference which corresponds to the white dashed line cross-section in (a)-(c). The grey filled region illustrates the extent of the bandgap.

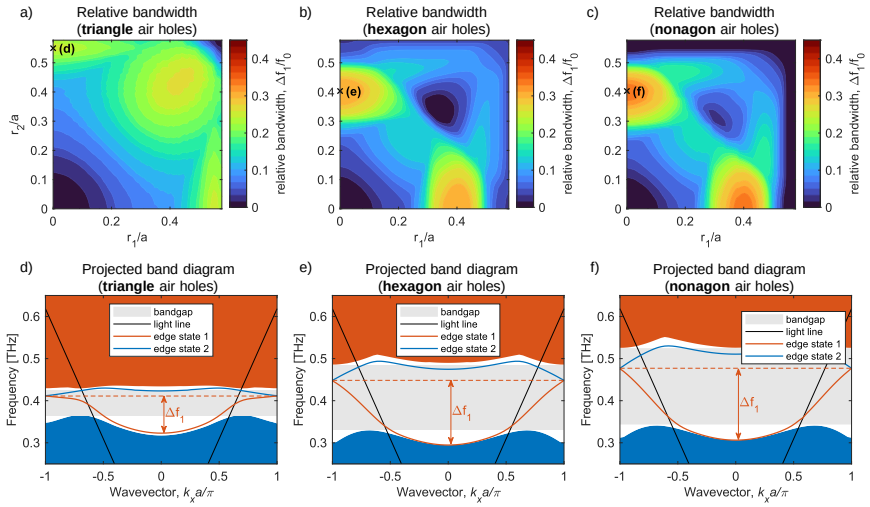

Fig. 4. Relative bandwidth of topological edge state for bearded-interface VPC waveguides as a function of air hole radii (r_1, r_2) for equilateral (a) triangular holes, (b) hexagonal holes, and (c) nonagonal holes. The relative bandwidth is given by $\Delta f_1/f_0$ where Δf_1 is the bandwidth spanned by the topological edge state and f_0 is the central frequency of the bandgap. (d-f) Projected band diagram corresponding to the marked data points in (a-c).

Figure 4 shows how the relative bandwidth ($\Delta f_1/f_0$) spanned by the topological edge state in bearded-interface VPC waveguides vary with the air holes shape (equilateral polygons with v vertices) and radii (r_1 and r_2). The variation of topological edge state relative bandwidth as a

Optics EXPRESS

function of the air hole geometry appears to follow similar trends with the VPC bandgap ratio. The relative bandwidth is enhanced for equilateral polygon air holes with 6 or more vertices and is maximized when one air hole is completely removed ($r_1 = 0$ or $r_2 = 0$). Note that the relative bandwidth spanned by the topological edge states shown in Fig. 4 are not necessarily within the bandgap, and only part of the topological edge states lying below the light line can support in-plane confined modes. Figure 5 shows the convergence of the bandgap ratio ($\Delta f/f_0$) and relative bandwidth ($\Delta f_1/f_0$) of a bearded-interface VPC waveguide towards the maximum value of 42% and 33%, respectively, by increasing the number of vertices of equilateral polygon air holes in a VPC rhombus unit cell with radii $r_1 = 0$ and $r_2 = 0.408$a.

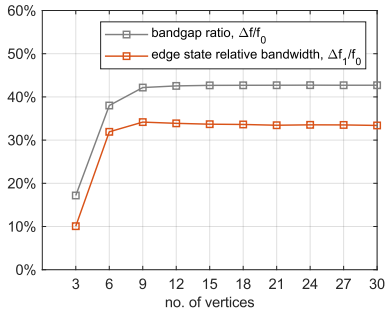

Fig. 5. Bandgap ratio of VPCs (grey) and edge state relative bandwidth for bearded-interface VPC waveguides (orange) plotted as a function of the number of vertices (v) for equilateral polygon air holes with radii $r_1 = 0$ and $r_2 = 0.408a$. The bandgap ratio converges toward 42% for $v \geq 12$, while the relative bandwidth converges toward 33% for $v > 12$.

2.4. *Composite interface junction for bearded-interface VPC waveguides*

While VPC waveguides with bearded-interface and a normal 120° bend has been shown to have negligible bending loss, the radii of air holes in such structures have always been limited by the condition $r < \frac{a}{2\sqrt{3}}$ such that they do not overlap [30,31]. Here we have shown that the relative bandwidth utilization of confined topological edge states can be increased by more than two folds via increasing the air holes size beyond the rhombus unit cell, albeit at the cost of physically separating the photonic crystal along the air-slot waveguide of the bearded-interface. Nonetheless, this issue may be circumvented by using the silicon on insulator (SOI) fabrication technology [29], or by designing a taper connecting the separated photonic crystal slabs [33].

In addition to the device and fabrication constraints, another limitation is the high bending loss encountered at the normal 120° bend of a bearded-interface with overlapping air holes (Fig. 2(a)) that forms an asymmetrical air-slot waveguide using dodecagon air holes with radii $r_1 = 0$ and $r_2 = 0.408a$ as shown in Fig. 6(a). This is due to the propagation of edge states along the domain wall (orange line), which allow the backwards coupling of wave at the bends (note that the domain wall can be traced backwards at the bends). To overcome this limitation, we design a 60° composite interface junction ("S" bend) with an unchanging bearded-interface by switching the unit cell type on either side of the domain wall after each interface junction (Fig. 6(b)).

Although the composite "S" bend introduces additional 120° bends at each interface junction, we show that up to 89 GHz bandwidth (~20% relative bandwidth) of the topological edge state is undisturbed by using a defective zigzag-interface as shown in Fig. 6(c). This is possible as the defective zigzag-interface supports an edge state (blue solid line) that only extends 25 GHz above the intersection between the topological edge state and light line (black dashed line). To demonstrate the robustness of the composite "S" bend, we simulate and show the magnetic field profile (H_z) excited using a unidirectional TE dipole array source for both the normal "Z" and

Optics EXPRESS

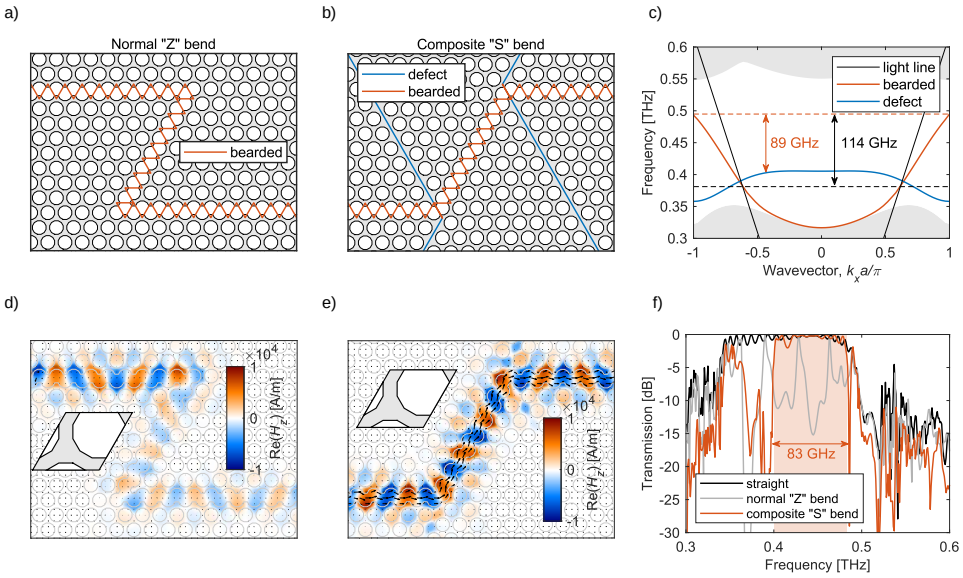

Fig. 6. Interfacial engineering for bearded-interface VPC waveguide with dodecagon air holes ($r_1 = 0$ and $r_2 = 0.408a$). (a) VPC waveguide with a normal "Z" bend between Type A and Type B unit cells and an unchanging bearded-interface. (b) VPC waveguide with a composite "S" bend with an unchanging bearded-interface connected to two 120° bends of defective zigzag-interface. (c) Projected band diagram showing the topological edge states supported by the bearded and defective zigzag-interface VPC waveguide. The composite "S" bend potentially allows unidirectional propagation of electromagnetic waves along the bearded-interface over a bandwidth of 89 GHz. (d), (e) Magnetic field profile (H_z) at 0.45 THz for the "Z" and "S" bend waveguide, respectively. The "Z" bend shows significant bending loss while the composite "S" bend shows near-unity transmission. (f) Comparison of transmission spectrum between the straight VPC waveguide as well as the VPC waveguides with the normal "Z" bend and composite "S" bend. The decrease in transmission due to coupling between the bearded and defective zigzag-interface at the composite interface junction of "S" bend VPC waveguide is apparent.

composite "S" bend waveguide at 0.45 THz frequency. Figure 6(d) shows electromagnetic wave propagation of high bending loss while Fig. 6(e) depicts a highly confined wave with negligible bending loss that propagates around the composite bend without coupling into the defective zigzag-interface. Furthermore, we simulate the transmission spectrum of both "Z" and "S" bend waveguides as shown in Fig. 6(f), with the composite "S" bend showing a near-unity transmission over 83 GHz bandwidth, corresponding to a 18.4% relative bandwidth.

3. Discussion

We have theoretically demonstrated a THz topological silicon waveguide with nearly 20% relative bandwidth utilization, with the potential to realize THz communication with data rates of up to 500 Gbit/s using a 90 GHz bandwidth and a 32-level quadrature amplitude modulation (QAM) [34]. In comparison with other all-silicon planar waveguides [35, 36], a topological waveguide with 30 GHz bandwidth can already achieve up to 135 Gbit/s data rate using 32-QAM [23] (see Table 1). However, the air-slot-like waveguide resulting from bearded-interface with large air holes poses some physical limitations. The fabrication of such silicon photonic device would result in two physically separated photonic crystal slabs, compromising the dimension and separation of the asymmetrical air-slot waveguide structure. One possible solution is to fabricate

Optics EXPRESS

the silicon photonic device on a SOI wafer using a top-down nanofabrication process which involves the patterning of the VPC structure on a photoresist using electron-beam lithography and employing inductively coupled plasma reactive ion etching (ICP-RIE) to etch the VPC structure on the top silicon layer of the SOI wafer [29]; Although this method of fabrication is costly and could reduce the usable bandwidth of topological edge states due to coupling with the SiO_2 substrate. An alternative method is to design a waveguide taper that connects the two separate pieces of photonic crystal slab to help facilitate the efficient coupling of THz waves into the VPC waveguide [33].

Table 1. Comparison of the relative bandwidth for all-silicon planar waveguides.

Reference	Type of waveguide	Frequency range (GHz)	Relative bandwidth (%)	Communication data rate	
				On-off keying modulation	32-level quadrature amplitude modulation
[10]	Photonic crystal	323-331	2.5	1.5 Gbit/s	-
[35]	Effective medium	260-400	42.4	30 Gbit/s	-
[36]	Unclad	260-390	~40	30 Gbit/s	-
[22,23]	Topological	320-350	~8	11 Gbit/s	135 Gbit/s
This work	Interfacial Topological	405-495	~20	-	up to 500 Gbit/s

Apart from the limitations imposed by the dispersion and bandwidth of topological edge state for the bearded-interface VPC waveguide with composite "S" bend, an avertible constraint is the edge state bandwidth of the defective zigzag-interface. Figure 7 show VPC waveguides with the standard zigzag-interface and the defect interface, as well as their corresponding projected band diagram. The defect interface is constructed by simply removing the "boat-shaped" polygonal air holes along the domain wall of the zigzag-interface, which effectively redshifts the topological edge state by about 11 GHz (see Fig. 7(c)). Further optimization of the domain wall interface via automatic differentiation [37] could potentially enable the bearded-interface to achieve full utilization of the 114 GHz bandwidth.

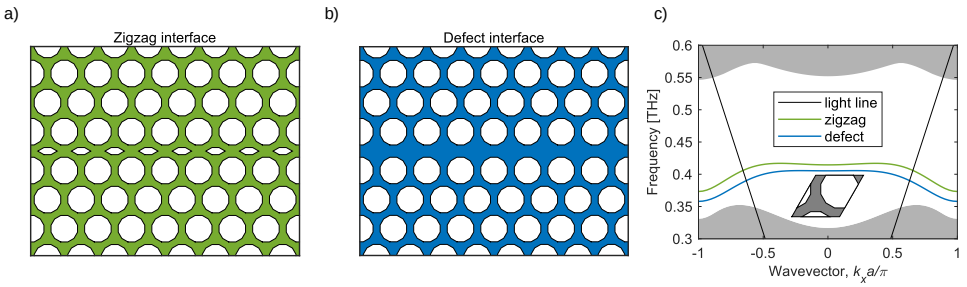

Fig. 7. VPC waveguides with: (a) zigzag-interface; (b) defect interface. The defect interface is obtained simply by completely removing the "boat-shaped" air holes of the zigzag-interface. (c) Projected band diagram of the VPC waveguides in (a) and (b), showing topological edge states of similar bandwidth centered at different frequency.

4. Methods

4.1. Plane wave expansion method for the computation of VPC band structures

The band structures of VPC unit cells and projected band diagrams of VPC waveguides are computed using the plane wave expansion (PWE) method, which reformulates the time harmonic

Optics EXPRESS

Maxwell's equations into an eigenvalue problem. The PWE method provides rigorous numerical solutions to Maxwell's equation with its accuracy limited only by the number of plane waves ($m_{\max}$, $n_{\max}$) used in the Fourier expansion of the dielectric function of a unit cell. Another advantage of the PWE method lies in the straightforward identification of eigenfrequencies of the bulk and edge states, making it easy to implement with optimization algorithms. For non-magnetic materials, the time harmonic Maxwell's equations can be expressed in a curl of curl relation given by

$$\frac{1}{\varepsilon_r(\mathbf{r})}\nabla\times(\nabla\times\mathbf{E}(\mathbf{r})) = \frac{\omega^2}{c^2}\mathbf{E}(\mathbf{r}) \tag{1a}$$

$$\nabla\times\left(\frac{1}{\varepsilon_r(\mathbf{r})}\nabla\times\mathbf{H}(\mathbf{r})\right) = \frac{\omega^2}{c^2}\mathbf{H}(\mathbf{r}) \tag{1b}$$

where $\mathbf{E}(\mathbf{r})$ and $\mathbf{H}(\mathbf{r})$ are the electromagnetic fields, $\varepsilon_r(\mathbf{r})$ is the relative permittivity, ω is the angular frequency and c is the speed of light in free space. For TE modes of a 2D VPC where $H_x = H_y = E_z = 0$, we can simply solve for the out-of-plane component of magnetic field H_z in equation Eq. (1b). By applying the curl of scalar product and curl of curl identities, Eq. (1b) can be reduced to an eigenvalue problem for the magnetic field H_z in 2D, described by

$$-\left[\frac{\partial}{\partial x}\left(\frac{1}{\varepsilon_r(\mathbf{r}_\parallel)}\frac{\partial}{\partial x}\right)+\frac{\partial}{\partial y}\left(\frac{1}{\varepsilon_r(\mathbf{r}_\parallel)}\frac{\partial}{\partial y}\right)\right]H_z(\mathbf{r}_\parallel) = \frac{\omega^2}{c^2}H_z(\mathbf{r}_\parallel) \tag{2}$$

In the PWE method, both the inverse dielectric function and the TE mode solution are expressed as a sum of plane waves along the reciprocal lattice vector in 2D, given by

$$\frac{1}{\varepsilon_r(\mathbf{r}_\parallel)} = \sum_{\mathbf{G}_\parallel}\chi(\mathbf{G}_\parallel)\exp(i\mathbf{G}_\parallel\cdot\mathbf{r}_\parallel) \tag{3a}$$

$$H_{z,\mathbf{k}_\parallel}(\mathbf{r}_\parallel) = \sum_{\mathbf{G}_\parallel}H_{z,\mathbf{k}_\parallel n}(\mathbf{G}_\parallel)\exp(i(\mathbf{k}_\parallel+\mathbf{G}_\parallel)\cdot\mathbf{r}_\parallel) \tag{3b}$$

with wavevector $\mathbf{k}_\parallel = k_x\hat{\mathbf{x}} + k_y\hat{\mathbf{y}}$, reciprocal lattice vectors $\mathbf{G}_\parallel = m\mathbf{b}_1 + n\mathbf{b}_2$ with reciprocal primitive vectors ($\mathbf{b}_1$, $\mathbf{b}_2$) and integers (m, n), $\chi(\mathbf{G}_\parallel)$ are the Fourier coefficients of the inverse dielectric function, and $H_{z,\mathbf{k}_\parallel n}(\mathbf{G}_\parallel)$ are the plane wave coefficients with wavevectors $\mathbf{k}_\parallel + \mathbf{G}_\parallel$. Substitution of Eqs. (3a) and (3b) into Eq. (2) leads to the following eigenvalue equation,

$$\sum_{\mathbf{G}'_\parallel}\chi(\mathbf{G}_\parallel-\mathbf{G}'_\parallel)(\mathbf{k}_\parallel+\mathbf{G}_\parallel)(\mathbf{k}_\parallel+\mathbf{G}'_\parallel)H_{z,\mathbf{k}_\parallel n}(\mathbf{G}'_\parallel) = \frac{\omega^2}{c^2}H_{z,\mathbf{k}_\parallel n}(\mathbf{G}_\parallel) \tag{4}$$

which allows the construction of an eigenmatrix to solve for the eigenfrequency ω and eigenstates $H_{z,\mathbf{k}_\parallel n}(\mathbf{G}_\parallel)$ for a finite number of plane wave components $-m_{\max}<m<m_{\max}$ and $-n_{\max}<n<n_{\max}$. To ensure convergence of simulation results, we have used up to 25 plane waves components ($m_{\max} = n_{\max} = 12$) for the computation of eigenfrequencies.

4.2. Particle swarm algorithm for topological edge state bandwidth optimization

The topological edge state bandwidth of the VPC waveguide is optimized by maximizing the objective function $F(v, r_1, r_2) = \Delta f\Delta f_1/f_0^2$ using the particle swarm algorithm, where v, r_1, r_2 are the number of vertices and radii of the equilateral polygon air holes in a unit cell (Fig. 1(a)). We employ a particle swarm algorithm described as follows:

```
for each particle i:
    for each parameter j=v, r1 and r2:
        Initialize particle's position xij, randomly drawn from a uniform distribution
```

Optics EXPRESS

```
        Initialize particle's best position to its initial position, p_ij ← x_ij
        Initialize particle's velocity to zero, Δx_ij = 0
while increase in F(b) is greater than 10^−6:
    for each particle i:
        for each parameter j = v, r1 and r2:
            Update particle's position, x_ij ← x_ij + Δx_ij
            Compute particle's function value, F(x_ij)
        Update particle's best position p_i ← x_i if F(x_i)>F(p_i)
        Update swarm best position b ← x_i if F(p_i)>F(b)
    for each particle i:
        for each parameter j = v, r1 and r2:
            Select random number ρ1 and ρ2 from a uniform distribution of [0,1]
            Update particle's velocity, Δx_ij ← wΔx_ij + c1ρ1(p_ij − x_ij) + c2ρ2(b − x_ij)
```

In this work, we set the boundaries of the particle swarm 3D search space to be $v \in [3,30]$ and $r_1, r_2 \in [0, a/\sqrt{3}]$, and used an inertia coefficient of $w = 0.5$, cognitive coefficient of $c_1 = 1.5$ and social coefficient of $c_2 = 1.5$. We find that a swarm of 64 particles are able to converge towards an optimal solution in less than 20 iterations.

4.3. Simulation of transmission spectrum for VPC waveguides

The 2D electromagnetic field profile and the transmission spectrum of the VPC waveguides are simulated in the frequency domain with the COMSOL Multiphysics Wave Optics Module, using an effective refractive index of $n_{\text{eff}} = 3.0$ to represent silicon of 200 μm thickness based on a variational method [27]. The VPC waveguide is artificially excited by a unidirectional TE source, simulated using an array of four electric point dipoles with spacing $a = 242.5$ μm and successive $2\pi/3$ phase shift placed along the air-slot waveguide with in-plane dipole moments perpendicular to the domain wall (see Fig. 8).

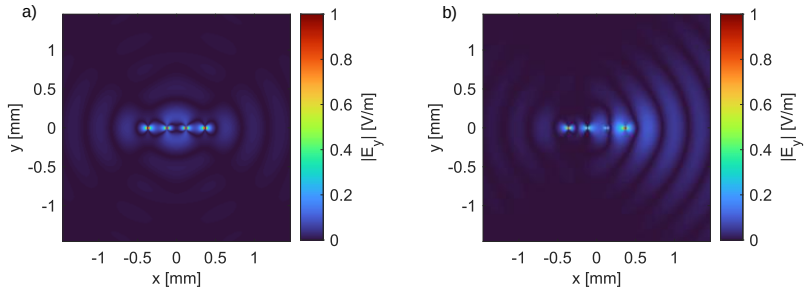

Fig. 8. The electric field $|E|$ distribution of four Hertzian dipoles spaced $a = 242.5$ μm apart at 0.45 THz frequency. (a) Hertzian dipoles that are radiating in phase results in radiation towards the both the negative and positive x-direction. (b) Hertzian dipoles with a successive $2\pi/3$ phase shift that simulates a unidirectional TE source.

The transmission ($T = P_{\text{out}}/P_{\text{total}}$) of VPC waveguides at each frequency is calculated by integrating the power flow across the air-slot waveguide output (P_{out}) and dividing it by the total power flowing out of the simulation domain (P_{total}).

5. Conclusion

We have theoretically demonstrated the opportunities and challenges of interfacial topological photonics for designing super broadband topological devices. The design approaches are scalable across the electromagnetic spectrum ranging from the microwaves to visible domain. As an

Optics EXPRESS

example, we showed a broadband topological silicon waveguide designed using VPCs with a bearded-interface that supports up to 25% relative bandwidth. By designing a composite interface junction for the asymmetrical air-slot-like VPC waveguide with the bearded-interface, we show that interfacial topological photonics offers the prospect of realizing broadband silicon waveguides that could support the robust topological transport of electromagnetic waves over a 20% relative bandwidth with linear dispersion. Our findings open a new perspective on the interfacial engineering of topological photonic systems to realize broadband topological devices for on-chip THz 6G communication.

Funding. National Research Foundation Singapore (NRF-CRP23-2019-0005).

Acknowledgments. YJ Tan acknowledges the A*STAR Graduate Scholarship funding from the Agency for Science, Technology and Research, Singapore. The authors also acknowledge the funding support from the National Research Foundation, Singapore (Grant No. NRF-CRP23-2019-0005).

Disclosures. The authors declare no conflicts of interest.

Data availability. Data underlying the results presented in this paper are not publicly available at this time but may be obtained from the authors upon reasonable request.

References

1. S. Dang, O. Amin, B. Shihada, and M.-S. Alouini, "What should 6G be?" Nat. Electron. **3**(1), 20–29 (2020).
2. I. F. Akyildiz, A. Kak, and S. Nie, "6G and Beyond: The Future of Wireless Communications Systems," IEEE Access **8**, 133995–134030 (2020).
3. Y. Lu and X. Zheng, "6G: A survey on technologies, scenarios, challenges, and the related issues," J. Ind. Inf. Integr. **19**, 100158 (2020).
4. S. Cherry, "Edholm's law of bandwidth," IEEE Spectrum **41**(7), 58–60 (2004).
5. T. S. Rappaport, Y. Xing, O. Kanhere, S. Ju, A. Madanayake, S. Mandal, A. Alkhateeb, and G. C. Trichopoulos, "Wireless Communications and Applications Above 100 GHz: Opportunities and Challenges for 6G and Beyond," IEEE Access **7**, 78729–78757 (2019).
6. X. You, C.-X. Wang, and J. Huang, *et al.*, "Towards 6G wireless communication networks: vision, enabling technologies, and new paradigm shifts," Sci. China Inf. Sci. **64**(1), 1–74 (2021).
7. P. Shumyatsky and R. R. Alfano, "Terahertz sources," J. Biomed. Opt. **16**(3), 033001 (2011).
8. Q. J. Gu, "THz interconnect: the last centimeter communication," IEEE Commun. Mag. **53**(4), 206–215 (2015).
9. K. Sengupta, T. Nagatsuma, and D. M. Mittleman, "Terahertz integrated electronic and hybrid electronic–photonic systems," Nat. Electron. **1**(12), 622–635 (2018).
10. K. Tsuruda, M. Fujita, and T. Nagatsuma, "Extremely low-loss terahertz waveguide based on silicon photonic-crystal slab," Opt. Express **23**(25), 31977–31990 (2015).
11. D. Guillaume, "Silicon photonics targets terahertz region," Nat. Photonics **12**(10), 574–575 (2018).
12. T. Harter, S. Muehlbrandt, S. Ummethala, A. Schmid, S. Nellen, L. Hahn, W. Freude, and C. Koos, "Silicon–plasmonic integrated circuits for terahertz signal generation and coherent detection," Nat. Photonics **12**(10), 625–633 (2018).
13. W. Withayachumnankul, M. Fujita, and T. Nagatsuma, "Integrated Silicon Photonic Crystals Toward Terahertz Communications," Adv. Opt. Mater. **6**(16), 1800401 (2018).
14. X. Yu, M. Sugeta, Y. Yamagami, M. Fujita, and T. Nagatsuma, "Simultaneous low-loss and low-dispersion in a photonic-crystal waveguide for terahertz communications," Appl. Phys. Express **12**(1), 012005 (2019).
15. A. B. Khanikaev and G. Shvets, "Two-dimensional topological photonics," Nat. Photonics **11**(12), 763–773 (2017).
16. A. B. Khanikaev, S. Hossein Mousavi, W.-K. Tse, M. Kargarian, A. H. MacDonald, and G. Shvets, "Photonic topological insulators," Nat. Mater. **12**(3), 233–239 (2013).
17. D. Bisharat, R. Davis, Y. Zhou, P. Bandaru, and D. Sievenpiper, "Photonic Topological Insulators: A Beginner's Introduction [Electromagnetic Perspectives]," IEEE Antennas Propag. Mag. **63**(3), 112–124 (2021).
18. M. Li, I. Sinev, F. Benimetskiy, T. Ivanova, E. Khestanova, S. Kiriushechkina, A. Vakulenko, S. Guddala, M. Skolnick, V. M. Menon, D. Krizhanovskii, A. Alù, A. Samusev, and A. B. Khanikaev, "Experimental observation of topological Z2 exciton-polaritons in transition metal dichalcogenide monolayers," Nat. Commun. **12**(1), 1–10 (2021).
19. S. Guddala, F. Komissarenko, S. Kiriushechkina, A. Vakulenko, M. Li, V. M. Menon, A. Alù, and A. B. Khanikaev, "Topological phonon-polariton funneling in midinfrared metasurfaces," Science **374**(6564), 225–227 (2021).
20. T. Ma and G. Shvets, "All-Si valley-Hall photonic topological insulator," New J. Phys. **18**(2), 025012 (2016).
21. J.-W. Dong, X.-D. Chen, H. Zhu, Y. Wang, and X. Zhang, "Valley photonic crystals for control of spin and topology," Nat. Mater. **16**(3), 298–302 (2017).
22. Y. Yang, Y. Yamagami, X. Yu, P. Pitchappa, J. Webber, B. Zhang, M. Fujita, T. Nagatsuma, and R. Singh, "Terahertz topological photonics for on-chip communication," Nat. Photonics **14**(7), 446–451 (2020).
23. J. Webber, Y. Yamagami, G. Ducournau, P. Szriftgiser, K. Iyoda, M. Fujita, T. Nagatsuma, and R. Singh, "Terahertz Band Communications With Topological Valley Photonic Crystal Waveguide," J. Lightwave Technol. **39**(24), 7609–7620 (2021).

Optics EXPRESS

24. K. Monika Devi, S. Jana, and D. Roy Chowdhury, "Topological edge states in an all-dielectric terahertz photonic crystal," Opt. Mater. Express **11**(8), 2445–2458 (2021).
25. S. Jana, K. Monika Devi, and D. Roy Chowdhury, "Effect of asymmetry on terahertz transmissions in topological photonic crystals comprising of dielectric rod structures," Opt. Commun. **505**, 127589 (2022).
26. R. A. S. D. Koala, M. Fujita, and T. Nagatsuma, "Nanophotonics-inspired all-silicon waveguide platforms for terahertz integrated systems," Nanophotonics **11**(9), 1741–1759 (2022).
27. M. Hammer and O. V. Ivanova, "Effective index approximations of photonic crystal slabs: a 2-to-1-D assessment," Opt. Quantum Electron. **41**(4), 267–283 (2009).
28. C. Wang, H. Zhang, H. Yuan, J. Zhong, and C. Lu, "Universal numerical calculation method for the Berry curvature and Chern numbers of typical topological photonic crystals," Front. Optoelectron. **13**(1), 73–88 (2020).
29. X.-T. He, E.-T. Liang, J.-J. Yuan, H.-Y. Qiu, X.-D. Chen, F.-L. Zhao, and J.-W. Dong, "A silicon-on-insulator slab for topological valley transport," Nat. Commun. **10**(1), 1–9 (2019).
30. H. Yoshimi, T. Yamaguchi, Y. Ota, Y. Arakawa, and S. Iwamoto, "Slow light waveguides in topological valley photonic crystals," Opt. Lett. **45**(9), 2648–2651 (2020).
31. X. Liu, L. Zhao, D. Zhang, and S. Gao, "Topological cavity laser with valley edge states," Opt. Express **30**(4), 4965–4977 (2022).
32. J. Kennedy and R. Eberhart, "Particle swarm optimization," in *Proceedings of ICNN'95 - International Conference on Neural Networks* (IEEE, 1995), **4**, pp. 1942–1948.
33. H. S. Dutta, A. K. Goyal, V. Srivastava, and S. Pal, "Coupling light in photonic crystal waveguides: A review," Photonics Nanostructures - Fundam. Appl. **20**, 41–58 (2016).
34. A. Pärssinen, M.-S. Alouini, M. Berg, T. Kürner, P. Kyösti, M. E. Leinonen, M. Matinmikko-Blue, E. McCune, U. Pfeiffer, and P. Wambacq, *White Paper on RF Enabling 6G–Opportunities and Challenges from Technology to Spectrum*, 6G Research Visions (University of Oulu, 2021).
35. W. Gao, X. Yu, M. Fujita, T. Nagatsuma, C. Fumeaux, and W. Withayachumnankul, "Effective-medium-cladded dielectric waveguides for terahertz waves," Opt. Express **27**(26), 38721–38734 (2019).
36. D. Headland, W. Withayachumnankul, X. Yu, M. Fujita, and T. Nagatsuma, "Unclad Microphotonics for Terahertz Waveguides and Systems," J. Lightwave Technol. **38**(24), 6853–6862 (2020).
37. M. Minkov, I. A. D. Williamson, L. C. Andreani, D. Gerace, B. Lou, A. Y. Song, T. W. Hughes, and S. Fan, "Inverse Design of Photonic Crystals through Automatic Differentiation," ACS Photonics **7**(7), 1729–1741 (2020).